






## Partial breakdown of translation symmetry at a structural quantum critical point associated with a ferroelectric soft mode

Y. Ishii <sup>1,\*</sup>, A. Yamamoto,<sup>2</sup> N. Sato <sup>3,4</sup>, Y. Nambu <sup>5,6,7</sup>, S. Ohira-Kawamura,<sup>8</sup> N. Murai,<sup>8</sup> K. Ohara <sup>9</sup>, S. Kawaguchi,<sup>9</sup> T. Mori <sup>3</sup> and S. Mori<sup>1</sup>

<sup>1</sup>Department of Materials Science, Osaka Metropolitan University, Sakai, Osaka 599-8531, Japan

<sup>2</sup>Department of Materials Science, Osaka Prefecture University, Sakai, Osaka 599-8531, Japan

<sup>3</sup>International Center for Materials Nanoarchitectonics (WPI-MANA), National Institute for Materials Science (NIMS), Tsukuba, Ibaraki 305-0044, Japan

<sup>4</sup>International Center for Young Scientists, NIMS, Tsukuba, Ibaraki 305-0047, Japan


<sup>5</sup>Institute for Materials Research, Tohoku University, Sendai 980-8577, Japan

<sup>6</sup>Organization for Advanced Studies, Tohoku University, 2-1-1 Katahira, Sendai 980-8577, Japan

<sup>7</sup>FOREST, Japan Science and Technology Agency, Kawaguchi, Saitama 332-0012, Japan

<sup>8</sup>Materials and Life Science Division, J-PARC Center, Tokai, Ibaraki 319-1195, Japan

<sup>9</sup>Japan Synchrotron Radiation Research Institute (JASRI), SPring-8, Sayo, Hyogo 679-5198, Japan

 (Received 13 June 2022; revised 31 August 2022; accepted 13 September 2022; published 27 October 2022)

We report that complete suppression of a phonon-driven structural phase transition causes partial breakdown of a three-dimensional translation symmetry in a well-defined sublattice. This state is revealed for a dielectric compound,  $\text{Ba}_{1-x}\text{Sr}_x\text{Al}_2\text{O}_4$ , that comprises an  $\text{AlO}_4$  network incorporated into a hexagonal  $\text{Ba}(\text{Sr})$  sublattice. Pair distribution function analyses and inelastic neutron scattering experiments provide clear-cut evidence of the  $\text{AlO}_4$  network forming a continuum of Al-O short-range correlations similar to glasses, whereas the  $\text{Ba}(\text{Sr})$  sublattice preserves the original translational symmetry. This glassy network significantly dampens the phonon spectrum and transforms it into the broad one resembling those typically observed in glass materials.

DOI: [10.1103/PhysRevB.106.134111](https://doi.org/10.1103/PhysRevB.106.134111)

### I. INTRODUCTION

Symmetry breaking in crystals has attracted broad interest in condensed matter physics. Particularly, exotic quantum phases in which spatial- or time-reversal symmetries are broken have been extensively studied over the last 20 years [1–7]. As a result, various fruitful research fields, such as topological insulators/superconductors, multiferroics, spintronics, and exotic superconductors, have been developed. Just as a point symmetry, a translation symmetry is also an essential component of crystals. However, few studies focus on a partial breaking of translation symmetry as a counterpart of point symmetry.

The aim of this study is to demonstrate that a three-dimensional translation symmetry is partially broken in a well-defined crystal by complete suppression of a soft-mode driven structural phase transition. The target material is  $\text{BaAl}_2\text{O}_4$ , which comprises an  $\text{AlO}_4$  tetrahedral network with six-membered cavities occupied by Ba atoms. This crystal structure is described as a combination of a Ba sublattice and an  $\text{AlO}_4$  network [Figs. 1(a) and 1(b)]. It experiences a structural phase transition [8] at  $T_C = 450$  K from the high-temperature phase (space group  $P6_322$ ) to the low-temperature phase ( $P6_3$ ) with an enlarged cell of  $2a \times 2b \times c$  [9]. Simultaneously, the Ba atoms slightly shift along the

$c$  axis, which gives a spontaneous polarization. This structural phase transition is driven by the acoustic soft mode (irreducible representation  $M_2$ ), whose vibration pattern is characterized as tilting of  $\text{AlO}_4$  accompanied by in-plane rotation of O1 atoms that connect the tetrahedra along the  $c$  axis [9]. Generally, in a soft-mode driven structural phase transition, the resultant low-temperature structure is closely related to the vibration pattern of the soft mode [10].

This acoustic soft mode is tunable by the chemical composition. As shown in the structural phase diagram (Fig. 2),  $T_C$  is rapidly suppressed by substituting Sr for Ba atoms and disappears near  $x = 0.1$  [11, 12]. For the composition window of  $0.1 \leq x \leq 0.5$ , characteristic honeycomb-type thermal diffuse scattering has been observed in electron diffraction patterns over a wide temperature range of at least 100–800 K. This fact means that the soft mode exists at very low frequencies or that a static structural fluctuation lies there. A further increase in  $x$  results in another structural phase transition to the  $P2_1$  phase at  $x = 0.55$ . Details of the structural phase diagram of  $\text{Ba}_{1-x}\text{Sr}_x\text{Al}_2\text{O}_4$  is reviewed in the Supplemental Material [13] together with the structural relationship between the parent  $P6_322$  phase and the low-temperature phases.

In this paper, we investigate the local structure and phonon spectra of  $\text{Ba}_{1-x}\text{Sr}_x\text{Al}_2\text{O}_4$  in the middle composition window. We show that complete suppression of the phonon-driven structural phase transition realizes a sublattice glass state in which the three-dimensional translation symmetry is partially broken in the well-defined crystal.

\*yishii@omu.ac.jp

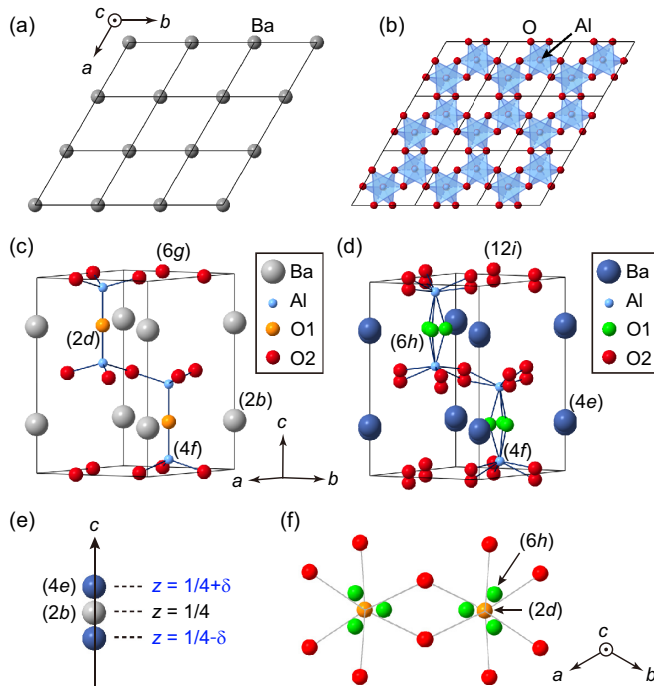


FIG. 1. Relationship between the (a) Ba sublattice and (b)  $\text{AlO}_4$  network of the high-temperature phase of  $\text{BaAl}_2\text{O}_4$  (space group  $P6_322$ ). Solid boxes indicate the multiple unit cells. (c) Ideal crystal structure of the high-temperature phase. The cell parameters determined by using laboratory x-ray diffraction are  $a = 5.2326(3)$  Å and  $c = 8.8174(7)$  Å at 500 K. (d) Split atom model used as an average structure model for  $x \geq 0.05$ . In this model, the Ba, O1, and O2 sites are split into several seats with lowered symmetries and partial occupancies. Panels (e) and (f) describe the relationship between the ideal and split positions of Ba and O1 atoms, respectively. (e) Ba atoms are accommodated at the  $2b$  site at  $z = 1/4$  in the ideal  $P6_322$  structure. When the Ba atoms have a small displacement ( $\pm\delta$ ) along the  $c$  axis from the ideal site, they can be accommodated at the  $4e$  site with lowered symmetry. (f) O1 atoms are accommodated at the  $2d$  site in the ideal structure. Al atoms are not shown here. Because the  $2d$  site is on the threefold axis along the  $c$  axis, the three seats of the  $6h$  site are generated in the split atom model.

## II. EXPERIMENT

Powder samples of  $\text{Ba}_{1-x}\text{Sr}_x\text{Al}_2\text{O}_4$  were synthesized using a conventional solid-state reaction. Powder x-ray diffraction was carried out at the BL02B2 beamline (SPring-8). The x-ray energy was set at 25 keV. X-ray total scattering measurements were carried out at room temperature at the BL04B2 beamline (SPring-8) with the x-ray energy of 113.2 keV. Multi-incident energy time-of-flight inelastic neutron scattering (INS) measurements were performed at AMATERAS [14] installed at BL14 in the Materials and Life Science Experimental Facility (MLF) in Japan Proton Accelerator Research Complex (J-PARC). The incident neutron energies were set at  $E_i = 52.45$ , 17.255, and 8.485 meV. For the inelastic neutron scattering experiment, the powder samples of  $x = 0, 0.03, 0.07, 0.2$ , and 0.3 (mass  $\approx 5$  g each) were separately enclosed in thin-walled aluminum cans with He exchange gas. A top-loading closed cycle refrigerator was used for temperature control. Obtained data were visualized using MSLICE [15] after data

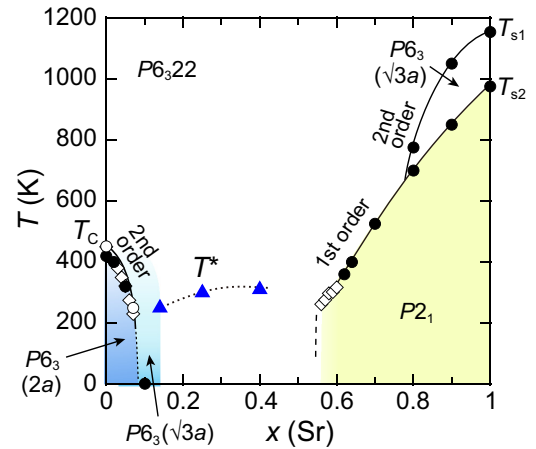


FIG. 2. Full phase diagram of  $\text{Ba}_{1-x}\text{Sr}_x\text{Al}_2\text{O}_4$  [9,11,12,22–24]. The phase boundaries are determined using powder x-ray diffraction (filled circles), synchrotron x-ray diffraction experiments for single crystals (open circles), and dielectric measurements (diamonds).  $T^*$  denotes the temperature at which thermal diffuse scattering caused by the  $M_2$  and  $K_2$  soft modes shows a maximum intensity. The  $K_2$  mode is another dominant soft mode in the high-temperature phase of  $\text{BaAl}_2\text{O}_4$ , and the  $P6_3(\sqrt{3}a)$  structure is the condensed state of the  $K_2$  mode [24]. The Supplemental Material provides further details of the phase diagram of  $\text{Ba}_{1-x}\text{Sr}_x\text{Al}_2\text{O}_4$  [13].

reduction [16].  $S(Q, E)$  were simulated using OCLIMAX [17] based on the phonon calculation. Phonon calculations were performed by using PHONOPY [18] in conjunction with density functional theory calculations using the Vienna *ab initio* package (VASP) code [19–21]. Thermal conductivity was measured for the densified polycrystalline samples of  $x = 0$ –1 using the steady-state method in a physical property measurement system (PPMS, Quantum Design). Further experimental details are included in the Supplemental Material [13].

## III. RESULTS

The synchrotron powder x-ray diffraction profiles at 15 K shown in Fig. 3(a) verify that the  $1/2 \ 3/2 \ 1$  superlattice reflection arising from the low-temperature phase is entirely suppressed in the composition window of  $0.06 < x < 0.1$ . The full width at half maximum (FWHM) is analyzed and converted to the correlation length ( $\xi$ ) in Figs. 3(b) and 3(c), respectively.  $\xi$  decreases with  $x$  and reaches  $\approx 20$  nm at  $x = 0.06$ . This variation reflects the microstructure being divided into smaller domains as  $x$  increases [23]. That is, the long-range order of the low-temperature phase is suppressed as  $x$  increases. Each domain is separated by antiphase boundaries in the  $ab$  plane [23,25]. The reported domain size is typically  $\approx 100$  nm at  $x = 0$ , decreases with increasing  $x$ , and reaches  $\approx 20$  nm at  $x = 0.07$  [23]. These values are consistent with the value of  $\xi$  shown in Fig. 3(c). The FWHM of the fundamental reflections are independent of the Sr composition and exhibit almost a constant value, as revealed by various diffraction methods [11,12].

The effect that changes the long-range order to short-range order should also affect the local structure of this material. Figure 4(a) displays the results of local structure analyses

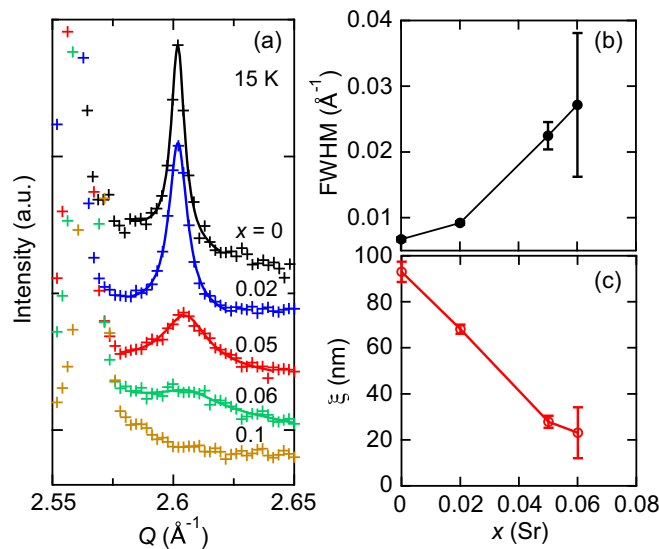


FIG. 3. (a) Synchrotron powder x-ray diffraction profiles in the range of  $Q = 2.55\text{--}2.65 \text{ \AA}^{-1}$  for  $\text{Ba}_{1-x}\text{Sr}_x\text{Al}_2\text{O}_4$  ( $x = 0\text{--}0.1$ ) samples at 15 K. The  $1/2 \ 3/2 \ 1$  superlattice reflection observed at  $Q \approx 2.6 \text{ \AA}^{-1}$  disappears between  $x = 0.06$  and  $0.1$ . (b) FWHM as a function of Sr composition ( $x$ ). (c) Correlation length ( $\xi$ ) converted from the FWHM value. The value of  $\xi$  decreases with  $x$  and reaches  $\approx 20 \text{ nm}$  at  $x = 0.06$ . This length corresponds to only  $\approx 20$  unit cells of the low-temperature phase.

for  $x = 0\text{--}0.3$  samples using the pair distribution functions (PDFs) [ $g(r)$ ] measured at 300 K. The profiles computed using the average structure models obtained with powder x-ray structural refinements [12] are also shown. The standard program package PDFGUI [26] was employed for the computation. Because of the structural phase transition, the structure model of the low-temperature phase ( $P6_3, 2a$ ) is employed as the average structure for the profile computation at  $x < 0.05$ . In contrast, the computation for  $x \geq 0.05$  employs the split atom model of  $P6_322$  [see Fig. 1(d)] as the average structure instead of the ideal structure [see Fig. 1(c)] because of the large atomic fluctuation. As shown in Fig. 4(a), the observed PDF profile for  $x = 0$  is well reproduced by the average structure model. Several characteristic peaks indicated by triangles are assigned based on the partial  $g(r)$  plotted at the bottom of Fig. 4(a); the peak at  $r \approx 1.75 \text{ \AA}$  comes from the Al-O1 and Al-O2 pairs in the  $\text{AlO}_4$  tetrahedra. The peaks observed at  $r \approx 3.45$  and  $6.80 \text{ \AA}$  correspond to the Ba-Al and Ba-Ba pairs, respectively. These pairs of atoms are indicated by double-headed arrows in the inset of Fig. 4(a).

The peak positions ( $r$ ) observed for  $x = 0$  at  $r \approx 1.75$ ,  $3.45$ , and  $6.80 \text{ \AA}$  are tracked and plotted as a function of  $x$  in Figs. 4(b)–4(d) together with the values calculated from the average structure models. The experimentally observed peak positions reflect the local structure of the compound. In the computed profile shown in Fig. 4(a), the O-O and Ba-O peaks are superimposed on each other at  $r \approx 2.9 \text{ \AA}$ . In addition, the computed peak at  $r \approx 2.9 \text{ \AA}$  is significantly broadened when  $x$  increases because of the Debye-Waller (DW) factors of Ba(Sr) and O atoms [12]. For these reasons, the position of the peak at  $r \approx 2.9 \text{ \AA}$  is not analyzed.

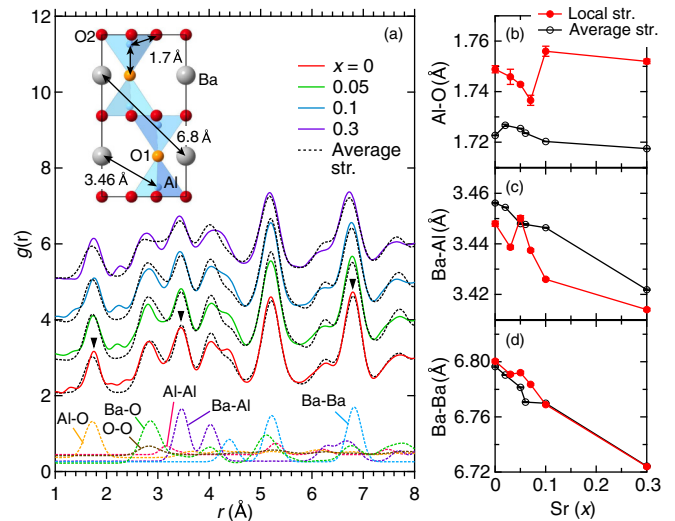


FIG. 4. (a) Experimentally derived PDFs [ $g(r)$ ] at 300 K of  $\text{Ba}_{1-x}\text{Sr}_x\text{Al}_2\text{O}_4$  with  $x = 0\text{--}0.3$  (solid curves). The  $g(r)$  curves for different compositions are plotted with a relative offset. Model calculations (broken curves) are also performed for each composition by using the average structures obtained with powder x-ray structural refinements [12]. Partial  $g(r)$  curves for the average structure of  $x = 0$  are shown at the bottom. The peak assigned as Al-O comes from the Al-O1 and Al-O2 correlations in the  $\text{AlO}_4$  tetrahedra. (b), (c), and (d) Peak positions of the Al-O, Ba-Al, and Ba-Ba correlations, respectively.

As shown in Fig. 4(d), the calculated peak positions of the Ba(Sr)-Ba(Sr) pair almost linearly decrease with increasing  $x$ , reflecting the variation in the lattice constant [11]. The experimentally observed peak positions of the Ba(Sr)-Ba(Sr) correlation are entirely consistent with those of the average structure models, indicating that the Ba(Sr) atoms are at the average position. A similar trend is also observed for the Ba(Sr)-Al pair, as shown in Fig. 4(c), although a small deviation is observed between the experimental and computational values. In contrast, the calculated values of the Al-O pair are almost independent of the Sr concentration, as shown in Fig. 4(b). In addition, the experimentally observed peak position of the Al-O pair exhibits a clear upshift at  $x = 0.1$ . This Al-O peak is well separated from the other peaks, including the Ba-O peak at  $r \approx 2.9 \text{ \AA}$ . Therefore, the results shown in Figs. 4(b)–4(d) indicate that the local structure of  $\text{AlO}_4$  tetrahedra deviates from the average structure at  $x \geq 0.1$ .

To investigate the nature of phonons, inelastic neutron scattering was performed on the powder samples. Figure 5(a) presents the contour plot of the dynamical structure factor [ $S(Q, E)$ ] for  $x = 0$  obtained at 100 K with incident energy  $E_i = 17.255 \text{ meV}$ . The calculated phonon dispersion for the  $P6_3$  low-temperature structure of  $x = 0$  is shown in Fig. 5(g). Figure 5(f) shows the simulated  $S(Q, E)$  based on the phonon calculation results. Overall, the simulation well reproduces the experimental result for  $x = 0$ . The prominent scattering intensity observed at  $\approx 5 \text{ meV}$  in Fig. 5(a) mainly comes from the optical phonons with a flat dispersion at the corresponding energies in Fig. 5(g). The weak streaks observed at  $2.5, 2.8, 3.2, 3.8,$  and  $4.2 \text{ \AA}^{-1}$  are ascribed to the dispersive acoustic modes at low energies.

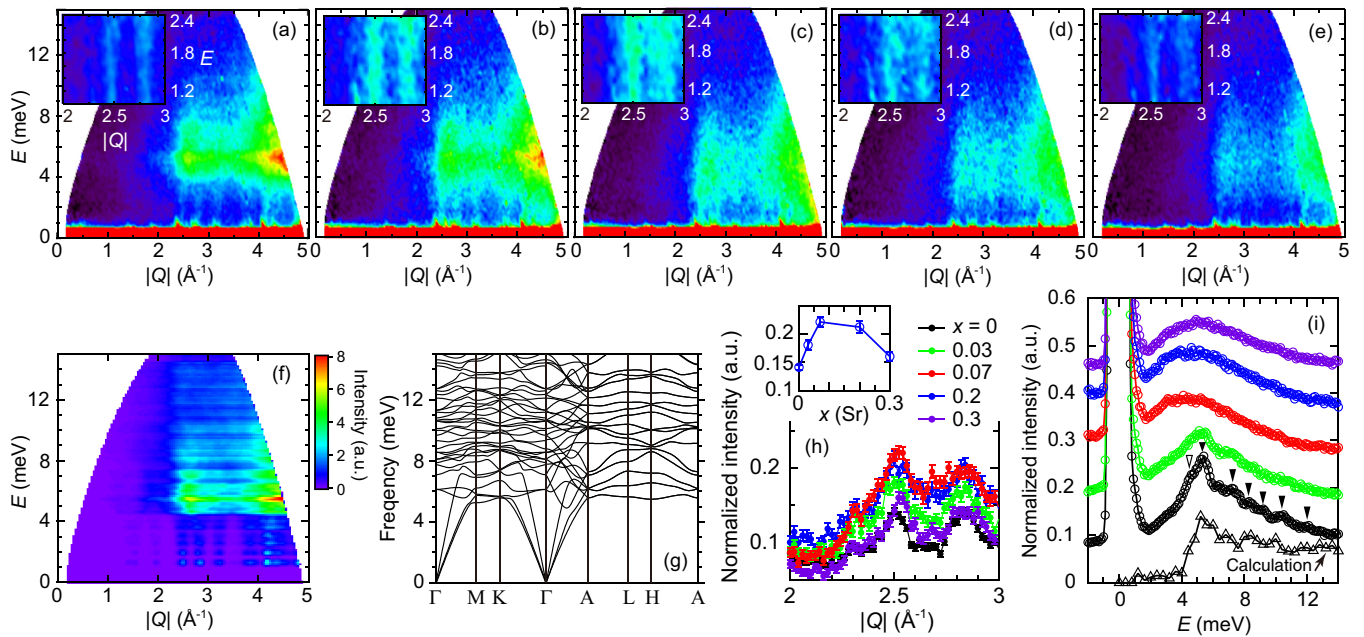


FIG. 5. Dynamical structure factor,  $S(Q, E)$ , for  $\text{Ba}_{1-x}\text{Sr}_x\text{Al}_2\text{O}_4$  powder samples of (a)  $x = 0$ , (b) 0.03, (c) 0.07, (d) 0.2, and (e) 0.3 measured at 100 K with  $E_i = 17.255$  meV. The insets show an enlarged view in the range of  $E = 1.0$ – $2.4$  meV and  $|Q| = 2$ – $3$   $\text{\AA}^{-1}$  obtained with  $E_i = 8.485$  meV. The Al sample can background has been subtracted from each scan. (f)  $S(Q, E)$  calculated using the OCLIMAX program [17] based on the phonon calculation for  $\text{BaAl}_2\text{O}_4$ . (g) Phonon-dispersion relations calculated on the ferroelectric  $P6_3(2a)$  structure of  $\text{BaAl}_2\text{O}_4$ . The calculation uses a  $2 \times 2 \times 3$  supercell of the unit cell. (h) Inelastic spectra energy integrated over the energy transfer  $E = 1$ – $2.3$  meV with  $E_i = 8.485$  meV. The inset presents the maximum intensity of the peak at  $Q \approx 2.5$   $\text{\AA}^{-1}$ . (i) Inelastic spectra  $Q$  integrated over  $|Q| = 2$ – $4$   $\text{\AA}^{-1}$  with  $E_i = 17.255$  meV. Profiles are offset by 0.09 for clarity. The intensities in panels (h) and (i) are normalized using a coherent cross section of the 111 nuclear peak whose structure factor is independent of the Ba/Sr ratio.

Interestingly, as shown in Figs. 5(b)–5(e), the energy distribution of the INS intensity deforms and shifts toward the lower-energy region as  $x$  increases. The insets of Figs. 5(a)–5(e) show the spectra in the low-energy region measured with  $E_i = 8.485$  meV. The intensity in the low-energy region exhibits an increasing trend toward  $x = 0.07$ . This trend is more explicitly observed in Fig. 5(h), where each spectrum is integrated over the energy transfer  $E = 1$ – $2.3$  meV. To discuss the intensities quantitatively, they are normalized using a coherent cross section of the 111 nuclear peak. Two peaks at  $Q = 2.5$  and  $2.8$   $\text{\AA}^{-1}$  arise from the acoustic modes, and the intensities strongly depend on  $x$  and show the largest value near  $x = 0.07$ . In the inset, the intensity at  $Q \approx 2.5$   $\text{\AA}^{-1}$  is plotted as a function of  $x$ . After showing a maximum near  $x = 0.07$ , it decreases with increasing  $x$ .

Figure 5(i) shows the  $S(E)$  with  $E_i = 17.255$  meV integrated over  $|Q| = 2$ – $4$   $\text{\AA}^{-1}$ . The calculation well reproduces the experimental result for  $x = 0$ . Several peaks, indicated by filled triangles, arise from the optical modes. In addition, the most prominent peak has a shoulder, as indicated by an open triangle, which is ascribed to the acoustic modes. At  $x = 0.03$ , the sharp peaks arising from the optical modes are significantly smeared out. They entirely disappear at  $x = 0.07$ , and the spectrum shows a broad character.

The glassy nature observed in the INS spectra should also appear in the thermal conductivity,  $\kappa$ . Figures 6(a) and 6(b) show the temperature dependence of  $\kappa$ . Generally in crystals, it behaves as  $\kappa \propto T^\alpha$  ( $\alpha = 3$ ) at the lowest temperatures, followed by  $\kappa \propto \exp(E/T)$  at several 10 K, and accordingly

shows a peak at  $\approx 20$  K. This characteristic peak is clearly observed for the end members, as indicated by filled triangles in Figs. 6(a) and 6(b), both of which have the long-range structures of  $P6_3$  and  $P2_1$ , respectively (see also Fig. 2 and Fig. S2 in the Supplemental Material [13]). Values of 2.3 and 2.6 are yielded for the low-temperature exponent  $\alpha$  for  $x = 0$

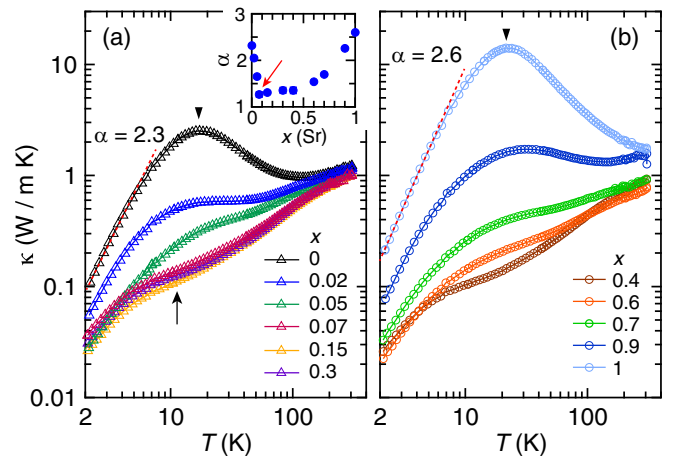


FIG. 6. Log-log plots of the thermal conductivity as a function of temperature for  $\text{Ba}_{1-x}\text{Sr}_x\text{Al}_2\text{O}_4$  of (a)  $x = 0$ – $0.3$  and (b)  $x = 0.4$ – $1$ . Error bars are smaller than the symbol size. Broken lines show the power fit using  $\kappa \propto T^\alpha$  for the experimental data of  $x = 0$  and  $x = 1$ . A plateau is observed for  $x = 0.07$ – $0.4$  near 10 K, as indicated by an arrow. The inset shows the power exponent  $\alpha$  plotted against  $x$ .

and 1, respectively. The smaller values than the ideal  $\alpha = 3$  are explained by the isotope effect [27]. The peak observed for  $x = 0$  is suppressed toward  $x = 0.07$  and entirely disappears above this composition. In the composition window of  $x = 0.07$ – $0.4$ , a plateau-like region appears, as indicated by an arrow, which is the typical characteristic observed in amorphous solids [28,29]. The large peak resurges as  $x$  increases further. That is, this plateau-like behavior is only observed in the middle composition range where the low-temperature structures are suppressed.

#### IV. DISCUSSION

The transition point where the structural phase transition occurs at  $T = 0$  has been known as the structural quantum critical point (sQCP) [30–32]. The complete suppression of the superlattice peak observed in Fig. 3(a) indicates that the sQCP lies in the composition window of  $x = 0.06$  and  $0.1$ . The absence of the structural phase transition has also been confirmed in dielectric measurements down to 2 K [23]. The inset of Fig. 6(a) summarizes the temperature exponent  $\alpha$  of the low-temperature  $\kappa$ . It shows a dip near  $x = 0.07$ , as indicated by an arrow in the inset. In addition, the low-temperature specific heat in our previous work considerably increases and exhibits a maximum near  $x = 0.1$ , and the Debye temperature ( $\Theta_D$ ) shows a dip [13,24].

The structural quantum material  $(\text{Sr}_{1-x}\text{Ca}_x)_3\text{Rh}_4\text{Sn}_{13}$  has also been reported to show a dip in  $\alpha$  and  $\Theta_D$  near the sQCP at  $x \approx 0.9$  [30,33]. In addition, the low-temperature specific heat of this system considerably increases toward the sQCP [34]. These characteristics are entirely consistent with those observed in the  $\text{Ba}_{1-x}\text{Sr}_x\text{Al}_2\text{O}_4$  system. Similar behavior has also been reported for the  $\Theta_D$  of  $\text{LaCu}_{6-x}\text{Au}_x$  near the sQCP at  $x \approx 0.3$  [31]. Thus, the observed behavior of the thermal parameters and the complete suppression of the superlattice reflection testify to the existence of the sQCP in  $\text{Ba}_{1-x}\text{Sr}_x\text{Al}_2\text{O}_4$ . The INS results shown in the inset of Fig. 5(h) indicate that the abundance of low-energy phonons should be the essential effect of the sQCP.

In the energy dependence of the INS spectrum for  $x = 0$  shown in Fig. 5(i), several peaks are observed at specific energies due to strong scattering by optical phonons. This peak structure disappears at  $x \geq 0.07$  and deforms into broad spectra resembling a boson peak commonly observed in amorphous solids [35–37]. That is, the broad spectra observed at  $x \geq 0.07$  indicate that glasslike static disorder is realized along with the long-range periodic structure.

Because the PDF analyses reveal that the Ba(Sr) atoms are at the average position, the glasslike disorder is ascribed to the  $\text{AlO}_4$  network in which the Al-O bond lengths deviate from the average value. This fact means that while Ba(Sr) atoms retain a rigid framework adapting to the  $P6_322$  symmetry, the  $\text{AlO}_4$  network forms a continuum of short-range correlations of  $\text{AlO}_4$  tetrahedra and partially breaks the translational symmetry at higher Sr concentrations than the sQCP. Because of this glassy Al-O network, the thermal conductivity for samples with  $x = 0.07$ – $0.4$  behaves as if they were amorphous solids. As described in the Introduction, the  $P2_1$  phase evolves at  $x > 0.5$ . As a result, the glassy network disappears, and thereby, the peak in the thermal conductivity reappears.

Generally, in crystalline solids, the phonon mean free path is so large at low temperatures that the value of  $\kappa$  varies with the number of phonons, which depends on temperature as  $\propto T^3$ . In other words, at low temperatures, more phonons should carry more heat, resulting in a larger value of the thermal conductivity. However, the thermal conductivity decreases toward the sQCP composition despite the increased number of low-energy phonons, as shown in Fig. 5(h). This contradiction indicates that the phonon mean free path decreases near the sQCP because of the glassy Al-O correlation, which likely suppresses phonon propagation.

The structural characteristic of this peculiar sublattice glass state can be understood as follows. Toward the sQCP composition, the microstructure of the ferroelectric phase is divided into small regions [23] with an average size of  $\approx 20$  nm [Fig. 3(c)]. At higher Sr concentrations than the sQCP, the soft mode presumably incoherently freezes inside the small islands, which has been observed in our previous transmission electron microscopy (TEM) experiments [11]. As shown in Fig. 1(e), the  $P6_322$  space group possesses the  $4e$  site above and below the  $2b$  site along the  $c$  axis. This  $4e$  site can accommodate the Ba(Sr) atoms even though the mode freezes incoherently and the atoms significantly deviate from the ideal position (the  $2b$  site). As a result, the local structure of the Ba(Sr) atoms coincides with the average structure described with the split atom model and preserves the periodicity across the crystal.

In contrast, the incoherently frozen O1 atoms cause a large displacement even from the  $6h$  site of the split atom model [Fig. 1(f)] because they are rotating around the  $2d$  site in the vibration of the soft mode. O1 atoms have been reported to exhibit an extremely large DW factor even in structural refinement using the split atom model, while O2 atoms exhibit a sufficiently small DW factor [12]. This large displacement from the  $6h$  site can reasonably be considered to be detected in the PDF analysis as a deviation from the average structure model. Such a local environment changes the  $\text{AlO}_4$  network from a long-range periodic structure to a continuum of Al and O correlations with various Al-O1 bond orientations, giving rise to the sublattice glass state in the  $\text{AlO}_4$  network. The atomic displacement of the Al atom is very small in the vibration pattern of the soft mode [9]. Accordingly, the DW factor of Al atoms does not largely increase in the Sr-incorporated samples [12]. This fact is also consistent with the picture of the incoherently frozen mode discussed above.

Figure 5(i) also indicates that the sublattice glass state significantly changes the nature of phonons of this material. Generally, the damping of phonons is large when the phonon lifetime is reduced, and larger damping gives broader phonon peaks in the phonon spectra. As shown in Fig. 5(i), all the phonon peaks indicated by triangles are smeared out with increasing  $x$  and thereby significantly broadened, indicating phonon damping. That is, the partial breakdown of the three-dimensional translational symmetry in the  $\text{AlO}_4$  network dampens all the phonons of  $\text{Ba}_{1-x}\text{Sr}_x\text{Al}_2\text{O}_4$ . Damping of phonons has been theoretically predicted to increase the low-energy vibration states [38,39], which is entirely consistent with our experimental observations.

Low-energy phonons have recently attracted increasing interest for layered thermoelectric materials with mobile ions

at high temperatures [40–42], which exhibit very low thermal conductivity due to the local vibration of the disordered interlayer ions. In the cage compounds, such as filled skutterudites and clathrate compounds [43,44], the so-called rattling mode is characterized as a localized Einstein mode with a certain vibration frequency of  $\approx 5$  meV [45], which also contribute to reduce thermal conductivity. In principle, the sublattice glass state revealed in this study is also applicable for other materials, including semiconductors and metals, with a tunable soft mode. Our findings should be a new strategy to explore low- $\kappa$  materials.

In the stream of studies focusing on the breakdown of spatial- and time-reversal point symmetry to explore exotic quantum phases, this work reveals that the translational symmetry can also be partially broken in crystals. Recent theoretical work has predicted that anharmonic phonon damping plays a key role in the superconducting dome at a ferroelectric quantum critical point [46]. The structural nature and the phonon damping observed in this study should pave a new path to pursue unusual quantum phases and phenomena in the future.

## V. CONCLUSIONS

By using the PDF analyses and INS measurements, we have demonstrated that short-range correlation with a broken

translational symmetry is realized at higher Sr concentrations than the sQCP of  $\text{Ba}_{1-x}\text{Sr}_x\text{Al}_2\text{O}_4$ . In this state, the  $\text{AlO}_4$  network forms a continuum of Al-O short-range correlations, while the original translational symmetry is preserved in the Ba(Sr) sublattice. Incoherent condensation of the soft mode at the sQCP is most likely responsible for this sublattice glass state. This state significantly dampens the phonons in the whole energy range, resulting in glassy thermal properties.

## ACKNOWLEDGMENTS

This work was supported by a JSPS Grant-in-Aid for Scientific Research on Innovative Areas “Mixed-anion” (Grants No. 16H06441, No. 17H05473, No. 17H05487, No. 19H04683, and No. 19H04704), JSPS KAKENHI (Grants No. 17H06137, No. 20H01844, No. 21H03732, and No. 22H05145), JST Mirai (Grant No. JPMJMI19A1), and JST FOREST (Grant No. JPMJFR202V). The synchrotron radiation experiments were performed at BL02B2 and BL04B2 of SPring-8 with the approval of the Japan Synchrotron Radiation Research Institute (JASRI) (Proposals No. 2015A1510 and No. 2020A1173). The INS experiments were performed at AMATERAS installed at BL14 in the Materials and Life Science Experimental Facility (MLF) in Japan Proton Accelerator Research Complex (J-PARC) (Proposal No. 2019B0022).

- 
- [1] M. Vojta, *Rep. Prog. Phys.* **66**, 2069 (2003).  
 [2] P. Gegenwart, Q. Si, and F. Steglich, *Nat. Phys.* **4**, 186 (2008).  
 [3] T. Giamarchi, C. Rüegg, and O. Tchernyshyov, *Nat. Phys.* **4**, 198 (2008).  
 [4] M. Smidman, M. B. Salamon, H. Q. Yuan, and D. F. Agterberg, *Rep. Prog. Phys.* **80**, 036501 (2017).  
 [5] S. Yip, *Annu. Rev. Condens. Matter Phys.* **5**, 15 (2014).  
 [6] N. Read and D. Green, *Phys. Rev. B* **61**, 10267 (2000).  
 [7] A. Y. Kitaev, *Phys. Usp.* **44**, 131 (2001).  
 [8] H. T. Stokes, C. Sadate, D. M. Hatch, L. L. Boyer, and M. J. Mehl, *Phys. Rev. B* **65**, 064105 (2002).  
 [9] Y. Ishii, S. Mori, Y. Nakahira, C. Moriyoshi, J. Park, B. G. Kim, H. Moriwake, H. Taniguchi, and Y. Kuroiwa, *Phys. Rev. B* **93**, 134108 (2016).  
 [10] M. T. Dove, *Structure and Dynamics* (Oxford University Press, New York, 2003).  
 [11] Y. Ishii, H. Tsukasaki, E. Tanaka, and S. Mori, *Sci. Rep.* **6**, 19154 (2016).  
 [12] S. Kawaguchi, Y. Ishii, E. Tanaka, H. Tsukasaki, Y. Kubota, and S. Mori, *Phys. Rev. B* **94**, 054117 (2016).  
 [13] See Supplemental Material at <http://link.aps.org/supplemental/10.1103/PhysRevB.106.134111> for (i) experimental details, (ii) a review of the phase diagram of  $\text{Ba}_{1-x}\text{Sr}_x\text{Al}_2\text{O}_4$ , and (iii) additional descriptions of the PDF profiles, INS spectra, specific heat, and thermal conductivity.  
 [14] K. Nakajima, S. Ohira-Kawamura, T. Kikuchi, M. Nakamura, R. Kajimoto, Y. Inamura, N. Takahashi, K. Aizawa, K. Suzuya, K. Shibata, T. Nakatani, K. Soyama, R. Maruyama, H. Tanaka, W. Kambara, T. Iwahashi, Y. Itoh, T. Osakabe, S. Wakimoto, K. Kakurai *et al.*, *J. Phys. Soc. Jpn.* **80**, SB028 (2011).  
 [15] R. T. Azuah, L. R. Kneller, Y. Qiu, P. L. W. Tregenna-Piggott, C. M. Brown, J. R. D. Copley, and R. M. Dimeo, *J. Res. Natl. Inst. Stand. Technol.* **114**, 341 (2009).  
 [16] Y. Inamura, T. Nakatani, J. Suzuki, and T. Otomo, *J. Phys. Soc. Jpn.* **82**, SA031 (2013).  
 [17] Y. Q. Cheng and A. J. Ramirez-Cuesta, *J. Chem. Theory Comput.* **16**, 5212 (2020).  
 [18] A. Togo and I. Tanaka, *Scr. Mater.* **108**, 1 (2015).  
 [19] G. Kresse and J. Hafner, *Phys. Rev. B* **47**, 558 (1993).  
 [20] G. Kresse and J. Furthmüller, *Comput. Mater. Sci.* **6**, 15 (1996).  
 [21] G. Kresse and J. Furthmüller, *Phys. Rev. B* **54**, 11169 (1996).  
 [22] Y. Ishii, H. Tsukasaki, S. Kawaguchi, Y. Ouchi, and S. Mori, *J. Solid State Chem.* **249**, 149 (2017).  
 [23] Y. Ishii, H. Tsukasaki, E. Tanaka, S. Kawaguchi, and S. Mori, *Phys. Rev. B* **94**, 184106 (2016).  
 [24] Y. Ishii, Y. Ouchi, S. Kawaguchi, H. Ishibashi, Y. Kubota, and S. Mori, *Phys. Rev. Mater.* **3**, 084414 (2019).  
 [25] A. M. Abakumov, O. I. Lebedev, L. Nistor, G. Van Tendeloo, and S. Amelinckx, *Phase Trans.* **71**, 143 (2000).  
 [26] C. L. Farrow, P. Juhás, J. W. Liu, D. Bryndin, E. S. Božin, J. Bloch, Th. Proffen, and S. J. L. Billinge, *J. Phys.: Condens. Matter* **19**, 335219 (2007).  
 [27] C. Kittel, *Introduction to Solid State Physics* (Wiley, New York, 1995).  
 [28] W. A. Phillips, *J. Non-Cryst. Solids* **31**, 267 (1978).  
 [29] J. J. Freeman and A. C. Anderson, *Phys. Rev. B* **34**, 5684 (1986).  
 [30] W. C. Yu, Y. W. Cheung, P. J. Saines, M. Imai, T. Matsumoto, C. Michioka, K. Yoshimura, and S. K. Goh, *Phys. Rev. Lett.* **115**, 207003 (2015).

- [31] L. Poudel, A. F. May, M. R. Koehler, M. A. McGuire, S. Mukhopadhyay, S. Calder, R. E. Baumbach, R. Mukherjee, D. Sapkota, C. de la Cruz, D. J. Singh, D. Mandrus, and A. D. Christianson, *Phys. Rev. Lett.* **117**, 235701 (2016).
- [32] S. U. Handunkanda, E. B. Curry, V. Voronov, A. H. Said, G. G. Guzmán-Verri, R. T. Brierley, P. B. Littlewood, and J. N. Hancock, *Phys. Rev. B* **92**, 134101 (2015).
- [33] X. Chen, Ph.D. thesis, University of Cambridge, 2017.
- [34] Y. Terasaki, R. Yamaguchi, Y. Ishii, Y. Tada, A. Yamamoto, and S. Mori, *J. Phys. Soc. Jpn.* **90**, 113704 (2021).
- [35] V. Malinovsky and A. Sokolov, *Solid State Commun.* **57**, 757 (1986).
- [36] T. Nakayama, *Rep. Prog. Phys.* **65**, 1195 (2002).
- [37] U. Buchenau, N. Nücker, and A. J. Dianoux, *Phys. Rev. Lett.* **53**, 2316 (1984).
- [38] M. Baggioli and A. Zaccone, *Phys. Rev. Lett.* **122**, 145501 (2019).
- [39] M. Baggioli and A. Zaccone, *Phys. Rev. Res.* **2**, 013267 (2020).
- [40] D. J. Voneshen, K. Refson, E. Borissenko, M. Krisch, A. Bosak, A. Piovano, E. Cemal, M. Enderle, M. J. Gutmann, M. Hoesch, M. Roger, L. Gannon, A. T. Boothroyd, S. Uthayakumar, D. G. Porter, and J. P. Goff, *Nat. Mater.* **12**, 1028 (2013).
- [41] K. Mizushima, P. C. Jones, P. J. Wiseman, and J. B. Goodenough, *Mater. Res. Bull.* **15**, 783 (1980).
- [42] B. Li, H. Wang, Y. Kawakita, Q. Zhang, M. Feyngenson, H. L. Yu, D. Wu, K. Ohara, T. Kikuchi, K. Shibata, T. Yamada, X. K. Ning, Y. Chen, J. Q. He, D. Vaknin, R. Q. Wu, K. Nakajima, and M. G. Kanatzidis, *Nat. Mater.* **17**, 226 (2018).
- [43] B. C. Sales, D. Mandrus, and R. K. Williams, *Science* **272**, 1325 (1996).
- [44] K. Suekuni, Y. Takasu, T. Hasegawa, N. Ogita, M. Udagawa, M. A. Avila, and T. Takabatake, *Phys. Rev. B* **81**, 205207 (2010).
- [45] R. P. Hermann, W. Schweika, O. Leupold, R. Ruffer, G. S. Nolas, F. Grandjean, and G. J. Long, *Phys. Rev. B* **72**, 174301 (2005).
- [46] C. Setty, M. Baggioli, and A. Zaccone, *Phys. Rev. B* **105**, L020506 (2022).